Bioactive Materials 36 (2024) 157–167

Contents lists available at ScienceDirect

Bioactive Materials

journal homepage: www.keaipublishing.com/en/journals/bioactive-materials

A multifunctional biomimetic nanoplatform for image-guideded photothermal-ferroptotic synergistic osteosarcoma therapy*

Yu-jie Liu [b,1], Su-he Dong [c,1], Wen-hao Hu [a,1], Qiao-ling Chen [a], Shao-fu Zhang [a], Kai Song [a], Zhen-chuan Han [c], Meng-meng Li [d,**], Zhi-tao Han [e,***], Wei-bo Liu [a,****], Xue-song Zhang [a,*]

[a] Department of Orthopaedics, The Fourth Medical Centre, Chinese PLA General Hospital, 51 Fucheng Road, Haidian District, Beijing, 100048, China
[b] Department of Orthopedic Oncology and Spine Tumor Center, Changzheng Hospital, Second Military Medical University, Shanghai, 200001, China
[c] PLA Rocket Force Characteristic Medical Center, Beijing, 100088, China
[d] Department of Anesthesiology, The Fourth Medical Centre, Chinese PLA General Hospital, 51 Fucheng Road, Haidian District, Beijing, 100048, China
[e] School of Integrated Chinese and Western Medicine, Nanjing University of Chinese Medicine, 210023, Jiangsu, China

A B S T R A C T

Much effort has been devoted to improving treatment efficiency for osteosarcoma (OS). However, most current approaches result in poor therapeutic responses, thus indicating the need for the development of other therapeutic options. This study developed a multifunctional nanoparticle, PDA-MOF-E-M, an aggregation of OS targeting, programmed death targeting, and near-infrared (NIR)-aided targeting. At the same time, a multifunctional nanoparticle that utilises Fe-MOFs to create a cellular iron-rich environment and erastin as a ferroptosis inducer while ensuring targeted delivery to OS cells through cell membrane encapsulation is presented. The combination of PDA-MOF-E-M and PTT increased intracellular ROS and LPO levels and induced ferroptosis-related protein expression. A PDA-based PTT combined with erastin showed significant synergistic therapeutic improvement in the anti-tumour efficiency of the nanoparticle in vitro and vivo. The multifunctional nanoparticle efficiently prevents the osteoclasia progression of OS xenograft bone tumors in vivo. Finally, this study provides guidance and a point of reference for clinical approaches to treating OS.

1. Introduction

Osteosarcoma, a rare form of cancer, accounts for approximately 0.2% of all cancer cases and 20% of primary bone cancers [1,2]. It typically affects the long bones of the body (e.g., the femur, tibia, or humerus) and has an incidence rate of 4.6 cases per million people per year in the USA, with a higher incidence in males, children, and young adults aged 10–25 years [2–4]. The most common symptom is bone pain, which may worsen with activity or at night and may also include swelling or tenderness in the affected area, limited movement, and a palpable mass occasionally [4,5]. The primary mode of treatment is surgical resection in combination with adjuvant chemotherapy to decrease the risk of local recurrence and metastatic disease, or with radiation therapy in cases where surgery is not feasible or for palliative purposes [6–8].

New treatment strategies for osteosarcoma have been a focus of recent studies [8]. Ferroptosis, identified by the accumulation of reactive oxygen species (ROS) and lipid peroxides within cells, is related to oncogenesis as well as cancer progression and osteosarcoma [9–11]. Suppression of glutathione peroxidase 4, a chief modulator of ferroptosis, can stimulate this cell death pathway and thwart osteosarcoma cell growth in vitro and in vivo [12]. Erastin, a small-molecule inducer of ferroptosis, triggers the depletion of intracellular glutathione due to cystine or glutamate antiporter inhibition, which leads to the accumulation of lipid peroxides and, ultimately, osteosarcoma cell death in vitro and in xenograft models [13]. Moreover, erastin combined with other therapies has been found to amplify the anti-tumour response in osteosarcoma. A recent study showed that simultaneous administration of erastin and doxorubicin enhanced the efficacy of doxorubicin and elicited ferroptosis in osteosarcoma cells [10,14]. Potential inducers of ferroptosis, such as Fe metal-organic frameworks (MOFs), have been investigated for their ability to generate reactive oxygen species (ROS)

* Peer review under responsibility of KeAi Communications Co., Ltd.
* Corresponding authors.
** Corresponding author.
*** Corresponding authors.
**** Corresponding author.
E-mail addresses: mml304@163.com (M.-m. Li), rkyyhzt@163.com (Z.-t. Han), liuweibo2011@163.com (W.-b. Liu), zhangxuesong301@126.com (X.-s. Zhang).
[1] These authors as co-first author contributed equally to this work.

https://doi.org/10.1016/j.bioactmat.2024.02.007
Received 8 December 2023; Received in revised form 6 February 2024; Accepted 7 February 2024

[15,16]. Fe-MOFs can trigger ferroptosis in cells by releasing iron ions that combine with hydrogen peroxide to generate hydroxyl radicals, leading to oxidative damage and lipid peroxidation [15–18].

Studies have shown the efficiency of Fe-MOFs in inducing ferroptosis in osteosarcoma cells and thus inhibiting their growth both in vitro and in vivo [17]. Furthermore, Fe-MOFs can work in synergy with erastin to induce ferroptosis in osteosarcoma cells. These studies have suggested the viability of the ferroptosis pathway for managing osteosarcoma [17], but additional studies are still needed to appraise the therapeutic potential and safety of ferroptosis inducers in treating osteosarcoma. Nevertheless, exploiting the ferroptosis pathway provides promising new avenues for developing innovative strategies to treat osteosarcoma [17].

The potential synergistic effects of combining PTT with ferroptosis inducers for cancer treatment have been recently explored [19–22]. PTT has emerged as a potential non-invasive and targeted approach for treating osteosarcoma, which employs NIR light-absorbing agents to generate heat and selectively ablate tumor cells [23–27]. The rationale for this combination is that PTT can enhance the accumulation of iron in cancer cells, making them more susceptible to ferroptosis induction [28,29]. Additionally, the heat generated by PTT increases lipid peroxidation, which is the key mechanism of ferroptosis [12,30–32]. Several preclinical studies have demonstrated the effectiveness of combining PTT with drugs such as erastin or RSL3 to induce ferroptosis in cancer cells [32]. Silica-coated iron oxide nanoparticles were used as a photothermal agent in a study to induce heat-mediated cell death, and erastin was then added to promote ferroptosis [33]. The combination treatment resulted in a synergistic effect, with greater cancer cell death compared to either treatment alone [33,34]. In another study, gold nanoparticles were used as a photothermal agent and combined with a ferroptosis inducer called ML162 [35]. It was found that the combination treatment led to increased lipid peroxidation and ROS production, resulting in enhanced cancer cell death [35]. Recently, polydopamine (PDA) nanoparticles have been found promising as delivery vehicles for cancer photothermal therapy due to their biocompatibility, stability, and ease of functionalization [18], which can be conveniently equipped with specific targeting molecules [36,37], such as antibodies or aptamers, to improve their specificity and selectivity towards cancer cells [36,38,39]. Considering the high surface area and tunable structures of MOFs, they can be integrated with PDA nanoparticles [40], thereby creating theranostic systems with enhanced imaging and therapeutic capabilities [41,42]. PDA can easily incorporate Fe-MOFs, improving its imaging and photothermal properties [43], and Fe-MOFs modified PDA nanoparticles exhibit excellent CT imaging contrast and selective NIR-aided targeting and elimination of osteosarcoma cells [44,45]. Additionally, they can also synergize with chemotherapy drugs to enhance their effect on destroying osteosarcoma cells [44].

Above all, how to combine and take advantages of multiple techniques to settle osteosarcoma down is the key point for this work. Herein, we reported a multifunctional nanoparticle, PDA-MOF-E-M, which was an aggregation of osteosarcoma targeting, programmed death targeting and NIR-aided targeting, all of which benefit from osteosarcoma membrane, MOF, erastin and PDA. The superiority of the physicochemical properties of PDA-MOF-E-M was identified and confirmed through the physical and biological characterization. Furthermore, the effects of PDA-MOF-E-M on the viability and fate of osteosarcoma cells were clarified in vitro, and its ability to induce ferroptosis in osteosarcoma treatment was also confirmed. In addition, the therapeutic effect of PDA-MOF-E-M on osteosarcoma-bearing mice was evaluated using allograft models. Overall, this work combined PTT with ferroptosis induction, providing a new attempt for the clinical treatment of osteosarcoma.

2. Results and discussion

2.1. Characterization of PDA-MOF-E-M

PDA-MOF-E-M is a nanomaterial that we designed and synthesized, combining the biological characteristics of PTT, ferroptosis induction, and osteosarcoma tumor targeting. According to published literature [46], it is constructed from a MOF iron skeleton, embedded with PDA nanoparticles, modified on the surface with erastin, and finally fused with osteosarcoma cell membranes. PDA is an excellent compound for PTT therapy because of its excellent photothermal properties and use of osteosarcoma cells' inherent thermal sensitivity to kill tumors [47]. MOF is a widely reported iron element nanoskeleton structure that can provide a locally rich iron element environment [16,48]. The erastin surface-modified by Michael's addition reactions, directly induces ferroptosis, causing osteosarcoma cells to die [10]. We then cultured osteosarcoma cells in vitro, isolated and extracted their cell membranes, and coated the synthesized nanoparticles in the cell membranes to improve the biocompatibility and targeting of the nanoparticles for bone tumors. Furthermore, we characterized the synthesized nanoparticles physically and biologically to validate their exceptional physicochemical properties. The SEM images revealed that the PDA-MOF-E-M and its synthetic raw materials (PDA and MOF) were uniform in shape, size, and dispersion and that the cell membrane's outer layer is visible (Fig. 1A, S1A-B). PDI analysis verified that PDA-MOF-E-M and its synthetic raw materials (PDA and MOF) had a unique nanoparticle size (with a similar average particle size of 100–1000 nm) and a narrow particle size distribution range, demonstrating the shape uniformity of the synthesized nanomaterials (Fig. 1B, S1C-D). Infrared spectroscopy was performed to identify the structural characteristics of nanoparticles, including PDA-MOF-E-M, PDA and MOF (Fig. 1C, S1E-F), in which PDA-MOF-E-M behaved similarly with the characteristics of PDA around 3421 cm^{-1} and 1651 cm^{-1}. Further, we measured the ultraviolet absorbance characteristics of nanoparticles at different synthesis stages and concentrations of PBS, PDA, MOF, PDA-MOF-E, and PDA-MOF-E-M between 350 and 750 nm (Fig. S1G). It is possible to classify the absorbance of different PBS concentrations as background noise because it was comparable. PDA and MOF exhibited completely different absorbance characteristics, and as the concentration of nanoparticles increased, so did their absorbance. PDA-MOF-E and PDA-MOF-E-M exhibited similar absorbance characteristics, with PDA contributing more to the changes in absorbance (Fig. S1G). However, it was evident that PDA-MOF-E-M exhibited superior ultraviolet absorbance characteristics at the same concentration (especially 50 μg/ml) (Fig. 1D). To take full advantage of this feature, we detected the stability of nanoparticles in acid-base (pH5.0 and pH9.0, Fig. S1H) and thermal (35 °C and 42 °C, Fig. S1I) stimulation, in which PDA-MOF-E-M, PDA and MOF behaved well in the aforementioned process, suggesting the favorable chemical stability for various humoral environments. Finally, we examined the biological characteristics of PDA-MOF-E-M nanoparticles and used Western blot to determine the effectiveness of cell membrane coating. By specifically detecting the protein types present in the cell membrane, represented by Na, K-ATPase α, it was observed that Na, K-ATPase was successfully detected in PDA-MOF-E-M (Fig. 1E). In contrast, none of proteins were detected in other nanoparticles, indicating that PDA-MOF-E-M was successfully coated with the cell membrane and had the corresponding biological activity. In this section, we experimentally confirmed the successful preparation of PDA-MOF-E-M nanoparticles and their exceptional physicochemical properties, indicating their potential as a therapeutic agent for osteosarcoma.

2.2. Ferroptosis induced by PDA-MOF-E-M

Next, the biological effects of PDA-MOF-E-M nanoparticles on the in vitro treatment of osteosarcoma were further validated. Oxidative stress levels are usually an important indicator evaluating the normality of cell

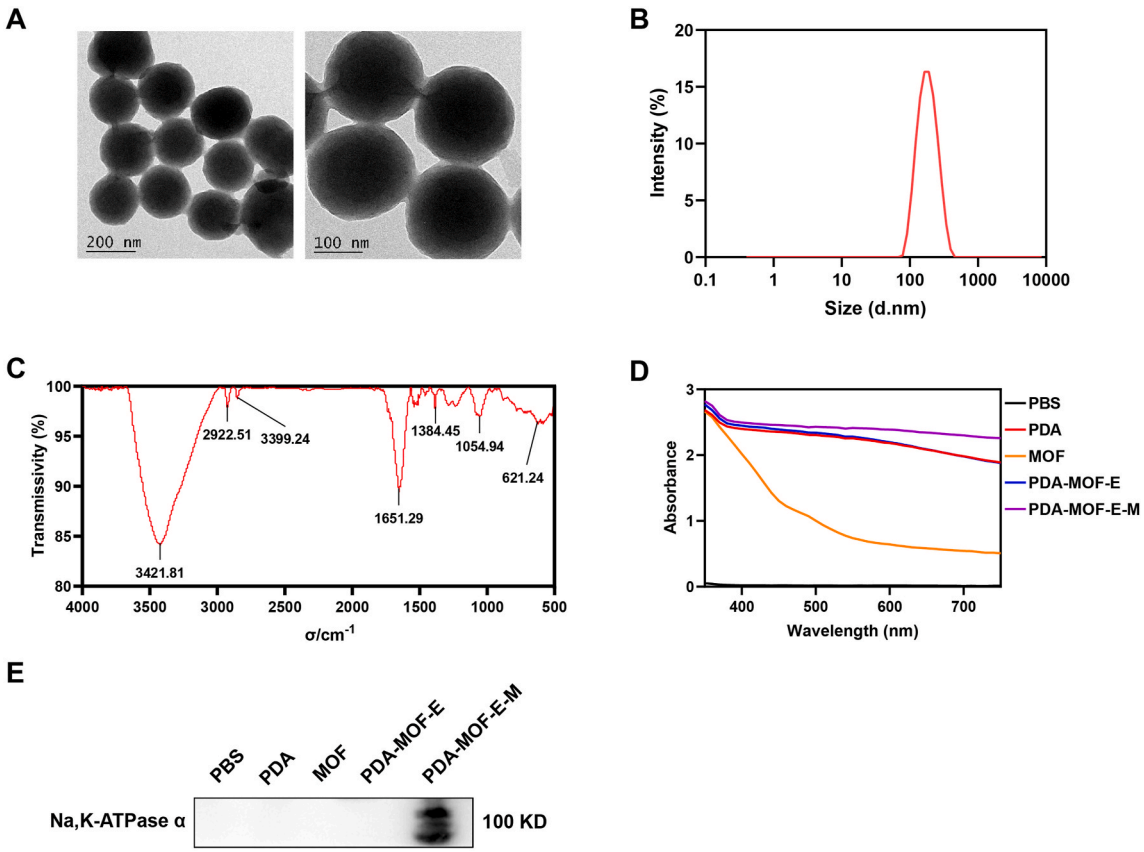

Fig. 1. Characterizations of PDA-MOF-E-M nanoparticles. (A) SEM images of PDA-MOF-E-M; (B) The size distribution of PDA-MOF-E-M; (C) Infrared spectrum of PDA-MOF-E-M; (D) UV–Vis spectra of PDA, MOF, PDA-MOF-E and PDA-MOF-E-M in concentration of 50 μg/ml; (E) The Western blot of PBS, PDA, MOF, PDA-MOF-E and PDA-MOF-E-M for protein concentration determination.

states, and excessive oxidative stress will inevitably lead to a series of malignant cell life activities, including ER stress, oxidative imbalance, inflammatory response, and programmed cell death [16,49,50]. Compared to the treatment of osteosarcoma cells by PBS, different nanoparticles or NIR therapy were all hereby found to lead to an increase in intracellular ROS levels (Fig. 2A). Among them, osteosarcoma cells treated with PDA-MOF-E-M + NIR presented the strongest ROS response, indicating the best efficiency of PDA-MOF-E-M in regulating the biological function of osteosarcoma cells (Fig. 2A). Furthermore, the impact of different treatments on the proliferation activity of bone tumor cells was also evaluated, which is the most direct indicator for the therapeutic effect of nanoparticles on osteosarcoma (Fig. 2B). The results showed that compared with PBS treatment, PDA treatment had almost no adverse effect on the vitality of osteosarcoma cells, while the treatment of other nanoparticles more or less inhibited the proliferation activity of osteosarcoma cells (Fig. 2B). Similar to the increase in the ROS levels, PDA-MOF-E-M also performed outstandingly in inhibiting osteosarcoma proliferation, almost inhibiting the proliferation of more than half of the cells. Besides, the iron content in cells is the first step in inducing cell death, a necessary condition for the formation of a ferroptosis microenvironment (Fig. 2C). The hereby-synthesized nanoparticles contain important sources of iron elements. To verify whether these nanoparticles can enter cells and release iron ions to form a rich iron microenvironment, the impact of different treatment methods on the change in iron content in osteosarcoma cells was detected as well, and the results showed that significantly different from PBS and PDA, MOF did provide sufficient intracellular iron-rich microenvironments (Fig. 2C). However, there was no significant statistical difference between PDA-MOF-E and PDA-MOF-E-M, proving that MOF could form a rich iron microenvironment in cells and that the doping of other nanoparticles and compounds exerted almost no significant impact on the iron content (Fig. 2D). Generally, cells are regulated by ferroptosis signals to undergo programmed cell death after forming a rich iron microenvironment, among which, lipid peroxidation is an important biological indicator of ferroptosis [51]. In this case, the impact of different treatment methods on lipid peroxidation in osteosarcoma cells was further detected (Fig. 2D), and the results showed that PBS and PDA treatment presented similar results, and the level of lipid peroxidation in osteosarcoma cells did not change significantly; even if MOF provided sufficient intracellular iron-rich environments, it did not lead to a significant increase in lipid peroxidation levels, indicating that the rich iron microenvironment in cells is only a necessary condition for ferroptosis, not a sufficient condition. Besides, the NIR therapy of both PDA-MOF-E and PDA-MOF-E-M led to a significant increase in lipid peroxidation in osteosarcoma cells, and almost no significant difference was observed between the two on this indicator, indicating the essential role of the ferroptosis inducer erastin in increasing lipid peroxidation levels in cells (Fig. 2D). Finally, the Western Blot method was used to detect the impact of different treatment methods on key regulatory molecules of the ferroptosis signaling pathway (Fig. 2E). Among them, SLC7A11 is a key regulatory protein of ferroptosis, also the specific target of erastin. Down-regulation of SLC7A11 leads to a decrease in the intracellular cysteine levels and a depletion of GSH biosynthesis, thus indirectly inhibiting the activity of GPX4, resulting in the accumulation of lipid peroxides, and ultimately inducing ferroptosis [13]. Compared with mesenchymal stem cells (MSCs), the expression of SLC7A11 and GPX4 is significantly overexpressed (Fig. S2A). Moreover, the high expression of SLC7A11 is closely associated with poor prognosis in sarcoma patients (Fig. S2B). In different treatments of osteosarcoma cells, compared with PBS, PDA treatment significantly increased the content of SLC7A11 and

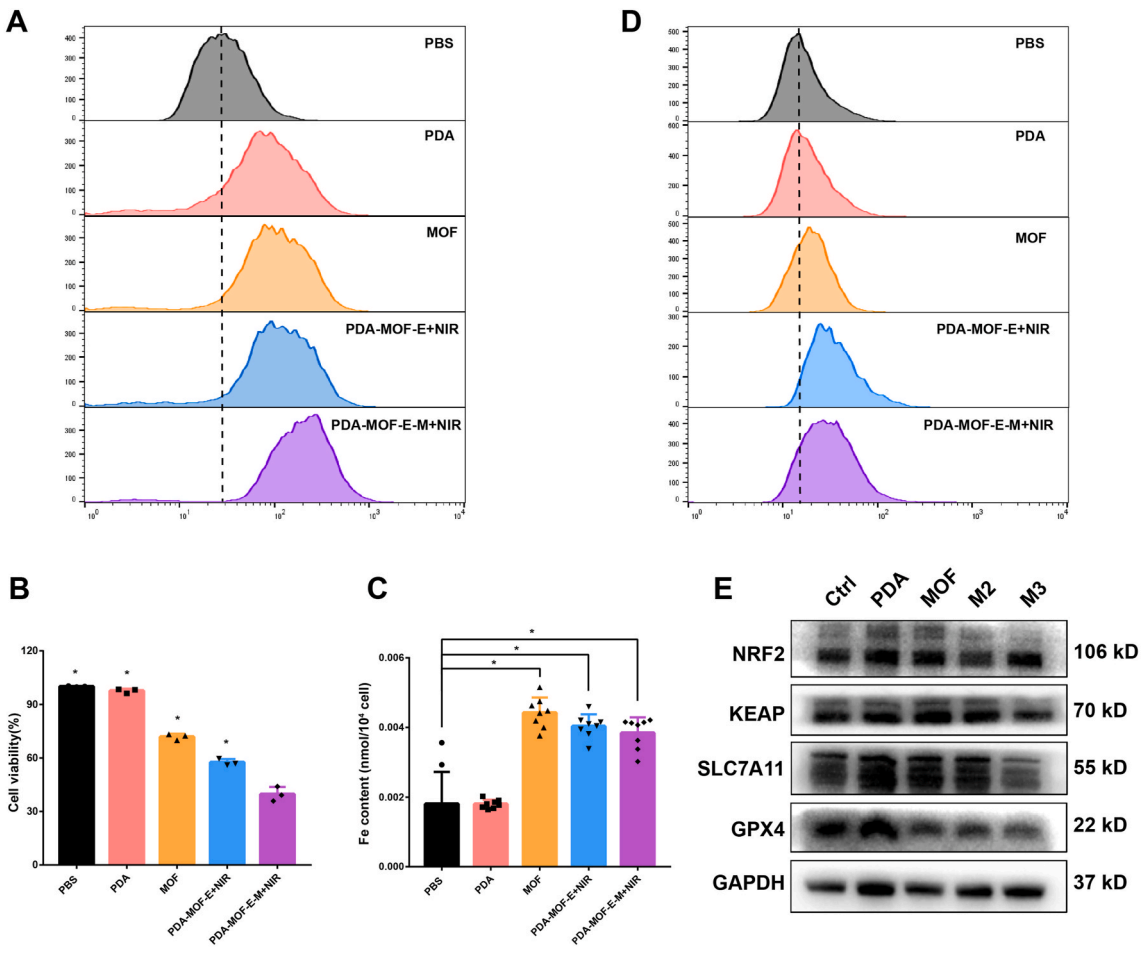

Fig. 2. PDA-MOF-E-M killed osteosarcoma cells via ferroptosis in vitro. (A) The ROS detection of PDA, MOF, PDA-MOF-E and PDA-MOF-E-M in 143B cells; (B) Cell viability determination of PDA, MOF, PDA-MOF-E and PDA-MOF-E-M in 143B cells; (C) Fe content determination of PDA, MOF, PDA-MOF-E and PDA-MOF-E-M in 143B cells; (D) The LPO detection of PDA, MOF, PDA-MOF-E and PDA-MOF-E-M in 143B cells; (E) The ferroptosis related proteins detection of PDA, MOF, PDA-MOF-E and PDA-MOF-E-M in 143B cells. *$p < 0.05$, **$p < 0.01$ and ***$p < 0.001$ analyzed by Student's t-test.

GPX4, which enhanced the ability of cells to resist ferroptosis (Fig. 2E). The results are consistent with the literature. Additionally, MOF, PDA-MOF-E + NIR, and PDA-MOF-E-M + NIR all inhibited the expression of GPX4 to varying degrees, indicating that the three methods all contribute considerably to inducing cell ferroptosis. Furthermore, PDA-MOF-E-M + NIR treatment effectively inhibited the expression of SLC7A11 in cells, while PDA-MOF-E + NIR treatment did not have a good inhibitory effect on the expression of SLC7A11, indicating the non-negligible contribution of cell membrane encapsulation to the delivery of PDA-MOF-E-M nanoparticles and erastin in cell activity (Fig. 2E). Under normal conditions, Keap1 maintains Nrf2 at low level by mediating Nrf2 ubiquitination and degradation. During the ferroptosis process, excess ROS degrades Keap1 and releases Nrf2 to compensate for excessive oxidative stress. Herein, PDA-MOF-E-M + NIR treatment significantly reduced the expression of Keap1 and significantly increased the expression of Nrf2, while other treatments showed no significant protein expression differences compared to PBS treatment, confirming that PDA-MOF-E-M + NIR treatment can promote the occurrence of ferroptosis in osteosarcoma cells.

2.3. Inhibition of osteoclast differentiation by PDA-MOF-Erastin

Osteosarcoma disrupts the homeostasis of the bone, and most bone diseases become osteolytic [5]. Osteosarcoma secretes osteoclast stimulating cytokines that stimulate bone resorption, and factors released during osteolysis promote tumor growth. RANKL (a member of the tumor necrosis factor TNF receptor family) and macrophage colony-stimulating factor (M-CSF) are two key factors required for osteoclast differentiation, especially required for osteoclast formation and function [52]. RANKL is provided with the capacity to suppress the function of inhibitory molecules in the upstream TRAF3 of NFATc1 induction, which can efficiently induce the NFATc1 auto-amplification [53,54].

It could be found that TRAF3 had an obvious increase in the mRNA expression level of OS cells with erastin administration in the dose-dependent mode (Fig. S2C). In order to demonstrate the inhibition capability of PDA-MOF-Erastin to osteoclastogenesis, the ability of osteoclast differentiation in bone marrow monocytes (BMMs) was hereby detected. BMMs were extracted from mice and induced by the addition of M-CSF (30 ng/ml) and RANKL (100 ng/ml). In the differentiation process, PBS, PDA, MOF and PDA-MOF-Erastin were respectively added to observe the effect of PDA-MOF-Erastin on osteoclasts. After treatment, the cells were stained according to the TRAP kit for identification. In the PDA-MOF-Erastin group, the differentiation of BMM osteoclasts, especially the formation of multinucleated osteoclasts, was found to be inhibited (Fig. 3A). Furthermore, the statistical results of osteoclasts also showed that the addition of PDA-MOF-Erastin could inhibit the formation of multinucleated osteoclasts (TRAP + cell >3 nuclei) (Fig. 3B). Besides, TRAF3 presented an obvious increase both mRNA and protein expression (Fig. 3C–E) with PDA-MOF-Erastin administration, while NFATc1 performed in an opposite manner. In a word, it demonstrates that PDA-MOF-Erastin can significantly inhibit

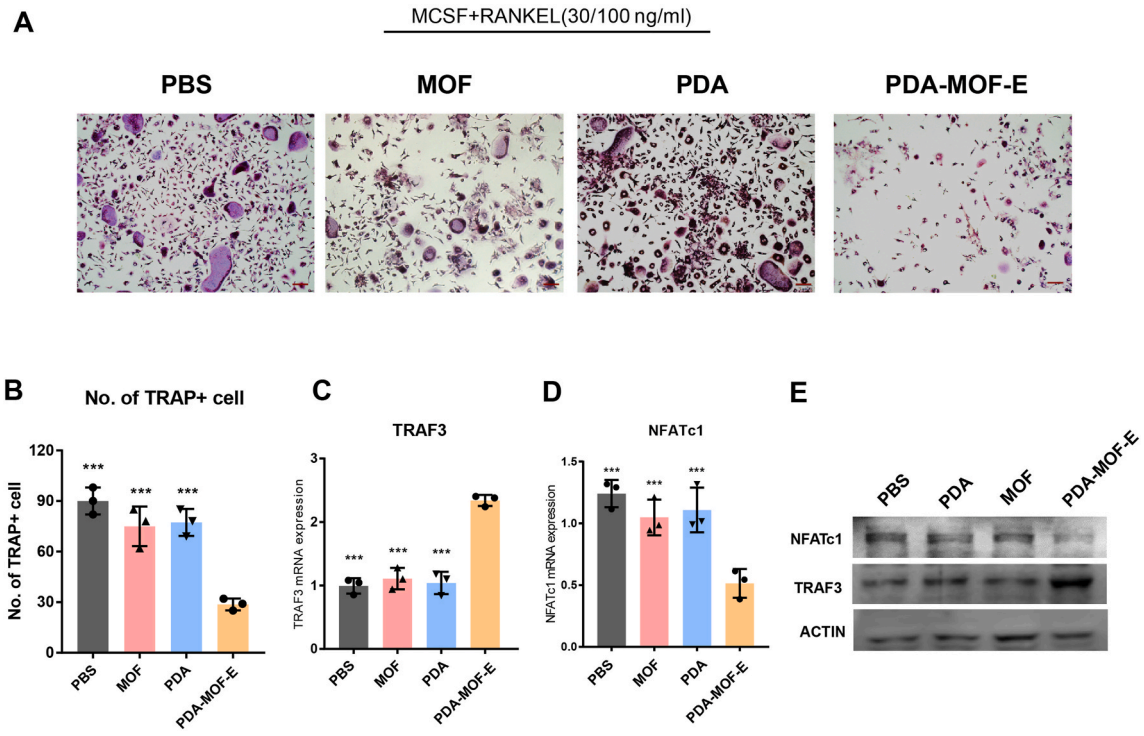

Fig. 3. PDA-MOF-E inhibits osteoclast differentiation. (A) TRAP staining images of osteoclastic differentiated BMMs. BMMs were pre-treated with M-CSF and RANKL (30/100 ng/ml) and incubated with PBS, PDA, MOF and PDA-MOF-E nanoparticles respectively; Scale bar, 50 μm; (B) The number of TRAP-positive multinucleated osteoclast cells with nuclei more than 3 after treatment was counted. Statistical analysis of TRAP positive multi-nucleated (≥3) osteoclasts in multiple field; (C–D) The mRNA expression level of osteoclast-specific genes including TRAF3 (C) and NFATc1 (D) in BMMs after the treatment; (E) WB assay to detect NFATc1 and TRAF3 expression. *p < 0.05, **p < 0.01 and ***p < 0.001 analyzed by Student's t-test.

osteoclast differentiation of BMMs.

2.4. Evaluation of the OS-targeting ability in vivo

In a previous study by the present group [55], a prepolymeric doping method was used to mix iron ion-(PDA) complex with free dopamine and polymerize PDA/Fe. The application of this method could adjust the loading efficiency of iron ions in a wider range, and PDA/Fe (loading 5.3% Fe ions) was chosen for high MRI contrast. To evaluate the contrast enhancement in MR, an investigation was conducted on the T1 relaxation rate of PDA/Fe in aqueous solution in a 7.0 T MR system. As the concentration of PDA/Fe decreased, the signal was observed to be weak in T1-weighted MR images (Fig. 4A–B). These results indicate that PDA/Fe can be used as positive contrast media.

For the diagnostic issue, the in vivo theranostic performance of PDA-MOF-E-M supramolecular nanomedicine in a tibia tumor bearing model was further investigated. PDA/Fe and PDA-MOF-E-M loaded with iron were prepared to evaluate the efficacy of OS-targeting therapy and distribution in vivo. Using a 7.0 T MR imager, T1 MRI was performed on mice with bone tumors before caudal venous injection and 24 h after caudal venous injection of PDA/Fe and PDA-MOF-E-M. The PDA-MOF-E-M group showed an enhanced T1 signal at the tumor site, while PDA/Fe injected mice showed no enhanced T1 signal. Analysis of T1 signal changes in tumor-associated bone showed an increase in the signal intensity in the area of bone injury after the injection of PDA-MOF-E-M compared to that before injection (Fig. 4C–D). The experimental results showed that PDA-MOF-E-M could be used as a contrast agent for the MRI of bone tumors, and the MR imaging signal of T1 in bone tumors of mice was significantly enhanced, which proved the efficiency of OS-membrane in enhancing the bone targeting of nanoparticles. Combined with the above results, it can be concluded that PDA-MOF-E-M has higher targeting of OS-tumors, and can be used as a nuclear magnetic resonance imaging contrast agent to guide the treatment of bone tumors.

2.5. Inhibition of OS growth in vivo

A tibial tumor mouse model was hereby established to evaluate the efficacy of PDA-MOF-E-M photothermal therapy combined with ferroptosis induction on bone tumor models in vivo (Fig. 5A). The mice with bone tumor were injected with PBS, PDA, MOF, PDA-MOF-E and PDA-MOF-E-M respectively through the caudal vein and irradiated with an 808 nm NIR laser. The temperature at the tumor site during NIR irradiation (1.0 W·cm-2, 5 min) was recorded using an infrared camera. The tumor site temperature of NIR irradiated mice was controlled near 43 °C (Fig. 5B), and the fluorescence images of mice were recorded before and after the synergistic treatment.

Among the three groups, including the PBS group, the MOF group and the PDA group, the fluorescence intensity of tumor was greatly increased after treatment. MOF showed a fairly strong fluorescence similar to PBS injection, which indicated that MOF failed to inhibit the growth of OS in vivo itself. NIR treatment was carried out in the three groups including the PDA, PDA-MOF-E and PDA-MOF-E-M group. In the PDA + NIR group, the relative fluorescence intensity was lower than that in the PBS group, but higher compared with the PDA-MOF-E and PDA-MOF-E-M group, indicating that the photothermal treatment alone could partially control the growth of bone tumor but could not completely inhibit it at 43 °C (Figs. S3A–B).

However, in the PDA-MOF-E and PDA-MOF-E-M + NIR group, the relative fluorescence intensity was lower than that in those three groups, demonstrating the inhibiting effect of erastin and photothermal treatment. Moreover, the PDA-MOF-E-M with NIR of PTT had the least intensity of fluorescence among the whole OS-bearing model mice after treatment, and photographs of the tumor in vitro after treatment showed similar results (Fig. 5C–D). This indicates that the introduction of OS-membrane can enhance the OS-targeting effect in the treatment and

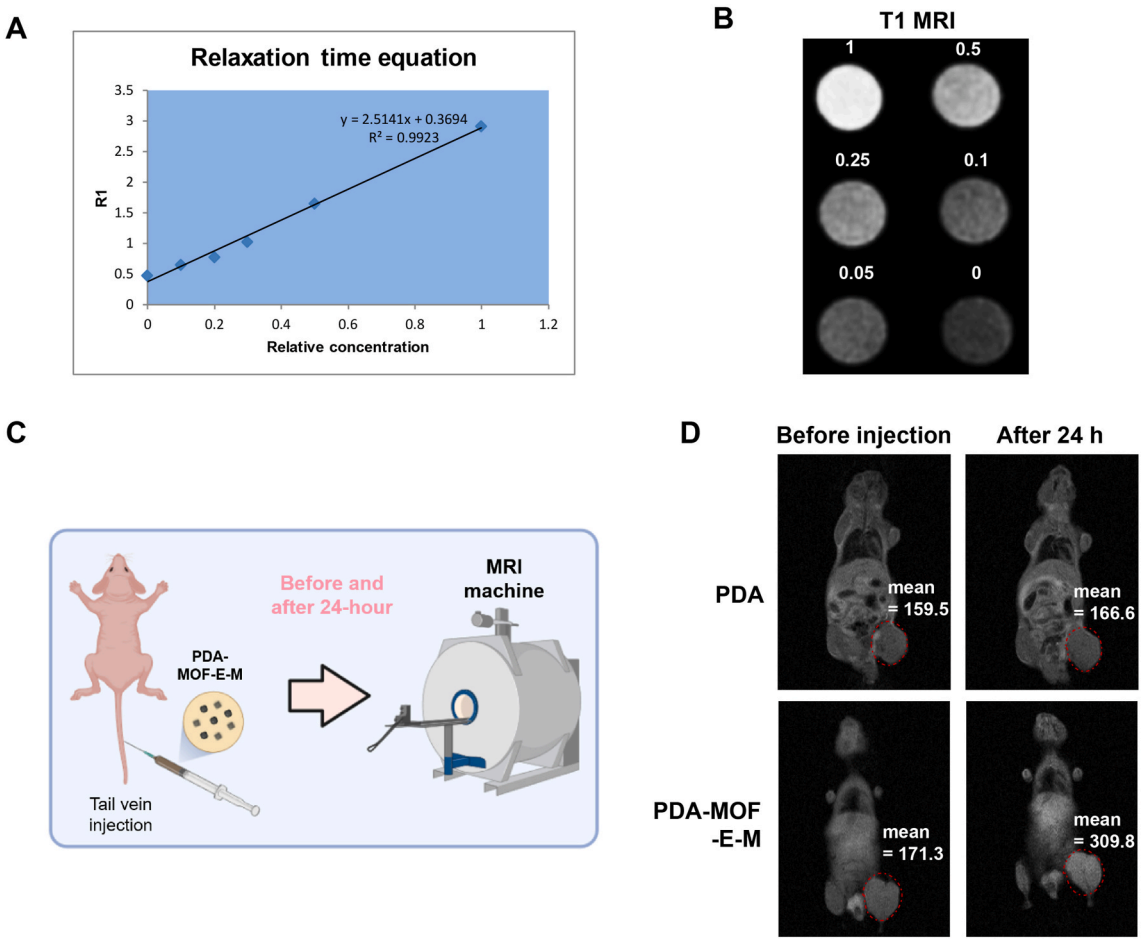

Fig. 4. MR images and biodistribution of PDA-MOF-Erastin-M. (A) Linear equation of relaxation time of PDA-MOF-Erastin-M; (B) T1-weighted magnetic resonance imaging of PDA/Fe images PDA-MOF-E-M at different concentrations in water; (C–D) T1-weighted MRI images of tibial tumor-bearing mice in vivo before and after intravenous injection of PDA/Fe and PDA-MOF-Erastin-M for 24 h and tibial tumors were indicated by red circle.

inhibit the growth of bone tumors at a relatively mild photothermal temperature, thus reducing tissue burns caused by an excessive photothermal temperature.

During the treatment, the tumor growth was almost completely inhibited in the PDA-MOF-E-M + NIR group, which, however, was inhibited but not completely inhibited in the PDA-MOF-E-M + NIR group. In addition, the difference of tumor volume and weight was detected and recorded to reflect the growth of bone tumor during treatment (Fig. 5E and Fig. S3C), and the results were consistent with those of tumor fluorescence intensity. Additionally, the body weight of mice in the treatment group did not change significantly during the treatment (Fig. S3D).

2.6. Inhibition of the osteolysis effect in vivo

The osteolysis and bone defect often occurred in OS tumorigenesis and progression [56]. To this end, OS-bearing model mice were thereby taken to confirm the ability of osteolysis remission to target the bones, in which the three-dimensional (3D) micro-computed tomography (micro-CT) was performed for further evaluation. The 3D micro-CT images showed that the tibia retained its morphological integrity in the PDA-MOF-E-M + NIR irradiated group compared to any other groups (Fig. 6A).

At the same time, the 3D parameters of the tibia, including the bone volume, bone surface area, bone trabecular number (Tb. N.) and bone trabecular separation (Tb. Sp.), were also evaluated, and the tendency of difference in the three indexes aforementioned was consistent with the above results. Especially, administration of PDA-MOF-E-M + NIR presented the maximal bone volume, the largest bone surface and the most trabecular numbers among the whole treatment groups (Fig. 6B–E). In general, the significantly stronger protective effect of the PDA-MOF-E-M + NIR irradiation group on the tibia microstructure compared with any other groups was clearly demonstrated.

Above all, the results indicated that the combination therapy of ferroptosis inducers and PTT with nanoparticles of OS-targeted administration could repress the growth of OS and relieve the osteolysis and bone defect in the OS-bearing model mice. Osteoclast differentiation had also been verified and monitored in the OS-bearing model mice after administration and irradiation treatments. The results were consistent with those in vitro, revealing that the expression of NFATc1 mRNA was decreased significantly after treating with both PDA-MOF-E-M administration and NIR laser irradiation and TRAF3 contrasted in the tendency of mRNA expression (Fig. 6F–G).

The toxicity of different treatments was further evaluated in vivo. No significant changes were observed in serum biochemical indicators including aminotranferease (ALT) aspartate aminotransferase (AST) levels and blood urea nitrogen (BUN) in the PDA-MOF-E-M treated mice (Figs. S4A–C). Besides, the histological staining of main organs including the heart, liver, spleen, lungs and kidneys was performed to detect the toxicity after administration of CPT in vivo, and the results suggested no obvious changes in aforementioned organs, implying the good biocompatibility, biodegradability and biosecurity of the NIR agents including PDA-MOF-E-M (Fig. S4D).

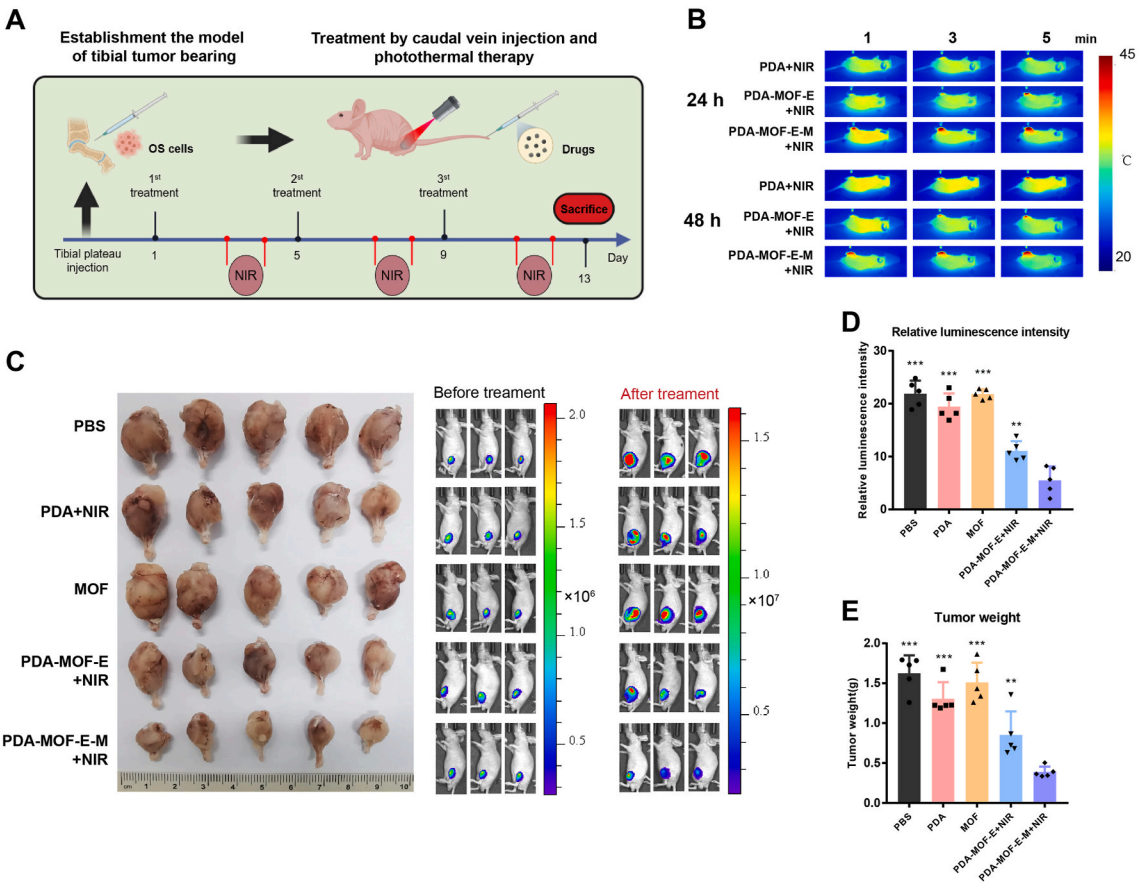

Fig. 5. In vivo treatment of tibia OS-bearing model. (A) Schematic diagram illustrates the process for PDA-MOF-E-M treatment and NIR irradiation; (B) Thermographs of mice taken at the end of NIR irradiation at 24 h and 48 h post-injection; (C) Luminescence images of tumor bearing mice and photographs of tibial tumors excised from mice. (D) The relative luminescence intensities of tibial tumors after treatment; (E) Average tumor weights of tibial tumors excised from mice. *$p < 0.05$ and ***$p < 0.001$ analyzed by Student's t-test.

3. Methods

3.1. Materials

Dopamine and DMF were both bought from Sigma-Aldrich (USA). NaOH and $FeCl_3{\cdot}6H_2O$ were purchased from Macklin Biochemical (China).

3.2. Synthesis of PDA

According to the literature-recommended method for synthesizing PDA, 90 mg of hydrochloride dopamine was dissolved in 45 ml of ultrapure water, vigorously stirred and heated to 50 °C. Then, 380 μL of 1 mol/L NaOH was added immediately. After 6 h of reaction, the solution was centrifuged at 11,000 rpm (25 min, 4 times) to remove excess reactants. Then, the precipitate was collected and dissolved in ultrapure water at 4 °C to obtain PDA.

3.3. Synthesis of Fe-MOF

According to the literature-reported method, Fe-MOF was hereby synthesized following the steps as follows: first, separately drop 10 mL of $FeCl_3{\cdot}6H_2O$ solution (H_2O, 40 mM) and 10 mL of BDC solution (DMF, 40 mm) into 25 mL of mixed solvent (DMF/water = 1/1) at a dripping rate of 50 mL/h and 15 mL/h, respectively. Then, take out 30 mL of reaction solution from the reaction bottle and repeat the above dripping operation five times. The obtained product was centrifuged and washed once with DMF, washed twice with anhydrous ethanol, kept moist, and then dried with nitrogen gas at room temperature for 20 min to obtain the final product.

3.4. Synthesis of PDA-MOF-E

1 mL of PDA solution, 1 mL of Fe-MOF solution, and 100 μL of erastin solution were taken, mixed thoroughly, and then shaken vigorously at room temperature for 2 h to obtain the PDA-MOF-E solution.

3.5. Preparation of osteosarcoma membrane

143B cells were collected in EP tubes and 0.1*PBS solution was added. After that, the EP tubes were transferred to liquid nitrogen and frozen for 8 s, and then transferred to room temperature to recover to liquid state. This freeze-thaw cycle was repeated 6 times and centrifuged at 14800 rpm for 10 min, and the supernatant was discarded. 1 mL of sterile water was added, homogenized by pipetting, and the obtained osteosarcoma membrane was stored at 4 °C.

3.6. Synthesis of PDA-MOF-E-M

1 mL of PDA-MOF-E was mixed evenly with 1 mL of 143B cell membrane. Following the recommended method in the literature, the mixture was treated with 37-degree ultrasound for 2 min, so as to ensure that the 143B cell membrane covered the surface of PDA-MOF-E fully and evenly. The system was then centrifuged at room temperature at 10,000 g for 5 min to remove the unloaded 143B cell membrane. The sediment obtained was PDA-MOF-E-M. 1 mL of sterile water was added

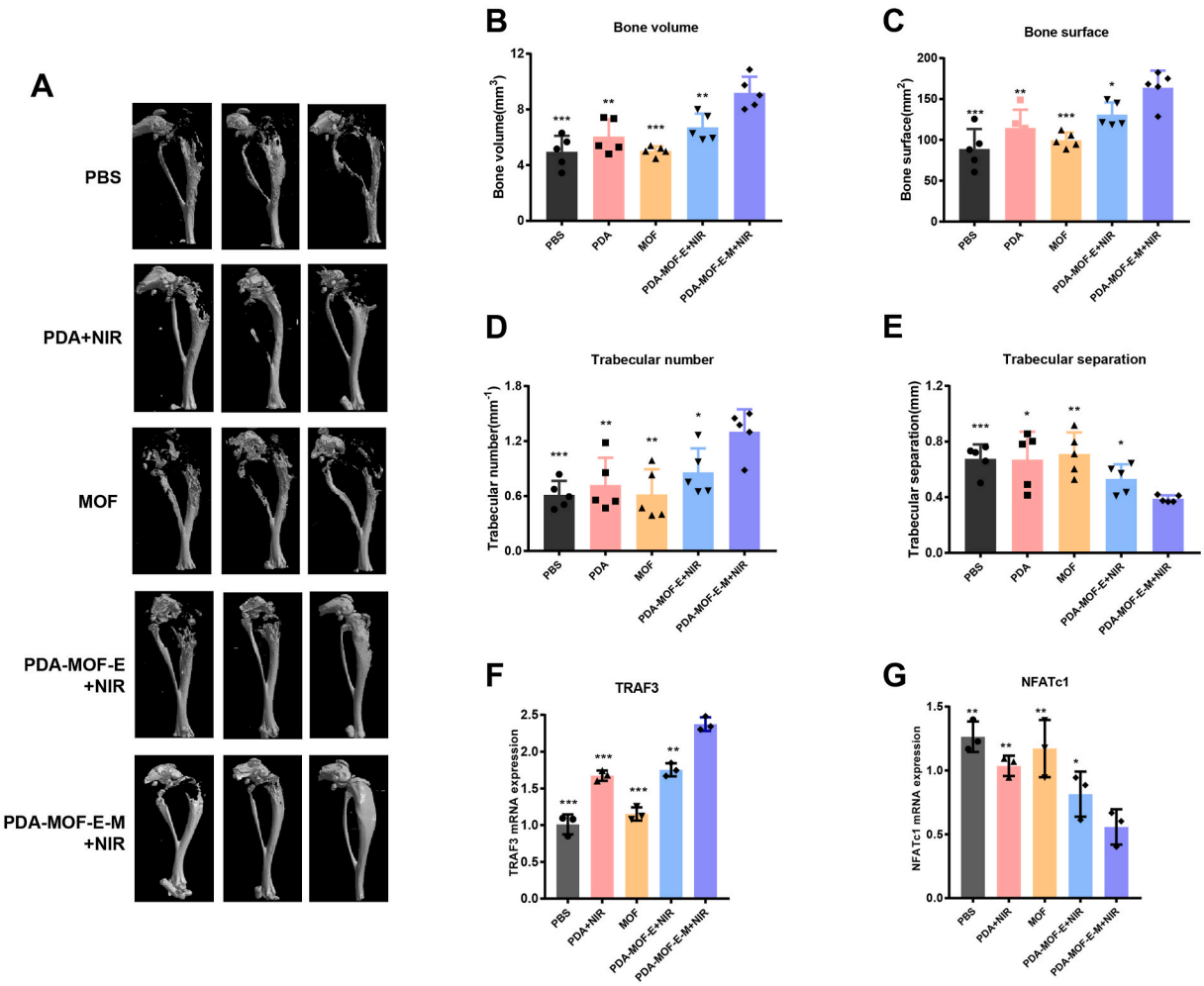

Fig. 6. The inhibition of osteolysis and osteoclast differentiation in osteosarcoma by PDA-MOF-E-M + NIR-mediated treatment. (A) 3D reconstructed image of tibias performed using micro-CT of OS-bearing mouse after treatment; (B–E) Quantitative analysis on the architecture parameters including bone volume, bone surface, trabecular number, and trabecular separation; (F–G) The mRNA expression level of osteoclast-specific genes including TRAF3 (F) and NFATc1 (G) in the tibial tissues after treatments by qRT-PCR. *p < 0.05 and ***p < 0.001 analyzed by Student's t-test.

to re-suspend the PDA-MOF-E-M, which was then stored at 4°.

3.7. Characterization of PDA-MOF-E-M

The morphology of PDA-MOF-E-M was observed using transmission electron microscopy (TEM), and the particle size distribution of PDA-MOF-E-M was measured using a dynamic light scattering instrument. The optical absorption spectra of nano-particles at different concentrations were evaluated using a UV–vis spectrophotometer. Assessing the cell membrane coating of PDA-MOF-E-M was followed the subsequent Western Blot assay.

3.8. Cell culture

143B cells were purchased from Wuhan Puno Life Science and Technology Co., Ltd. and cultured in DMEM medium supplemented with 10% fetal bovine serum and 1% penicillin-streptomycin. The cells were then placed in a cell culture incubator containing 5% carbon dioxide and cultured at 37 °C.

3.9. Western blot

According to cell density or tissue weight, lysis buffer and protease/phosphatase inhibitor mixture (100:1) was added, cell sonication or bead milling was performed, lysis was ice-cooled for 30 min and centrifuged at 14,000 g for 15 min, the supernatant was collected, the protein concentration was determined by BCA assay kit, and protein loading buffer was then added, which was then heated at 97 °C in a metal bath for 10 min. A rapid gel kit was used to prepare separation and concentration gels (10%) at a constant pressure of 200 V for 30 min. PVDF membrane was activated with methanol solution in advance, and then run at a constant current of 200 mA for 2 h, blocked with 5% milk in TBST and incubated at room temperature for 2 h. Primary antibody SLC7A11, GPX4, Nrf2 and Keap1 (1:1000, CST, USA) was incubated on a shaking bed at 4 °C overnight. The membrane was washed with TBST three times and incubated with secondary antibody at room temperature for 1 h. Then, the membrane was washed with TBST three times, and ECL developing solution was added and imaged with a chemiluminescence imager.

3.10. CCK-8 assay

The recommended method of the reagent manufacturer for CCK-8 assay was adopted. Specifically, 143 cells were seeded in a 96-well plate and incubated overnight. Different treatment methods were administered to stimulate the 143B cells, and after 12 h, the culture medium was removed and washed three times with PBS, and CCK-8 detection working solution was prepared by mixing the CCK-8 assay

reagent with culture medium at a ratio of 1:10. A total of 200 μL of CCK-8 detection working solution was added to each well and incubated for 2–4 h in a cell culture incubator, and the absorbance of the cells at 450 nm was measured using a UV spectrophotometer.

3.11. ROS and LPO assay

143B cells were seeded in a 6-well plate and cultured overnight. The treated 143B cells were stimulated with different therapeutic methods. After 12 h, the processed 143B cells were washed twice with HBSS solution. 10 μmol/L H2DCFDA (used for ROS detection) or C11 BODIPY 581/591 (used for LPO detection) was mixed with HBSS (1:1000) and incubated at 37 °C for 30 min, which was then washed three times with HBSS solution. The 1640 culture medium was preheated and incubated at 37 °C for 20 min. The flow cytometer was used to detect the ROS and LPO levels in cells under a wave length of 495/529 nm.

3.12. MRI of PDA/Fe and PDA-MOF-E-M in vivo

BALB/c nude mice (4 weeks old) with an average weight of 20 g were purchased from SLAC Laboratory Animal Co. Ltd. (Shanghai, China). The animal experiments were carried out according to the National Institutes of Health guidelines for care and use of laboratory animals and approved by the ethics committee of Chinese PLA General Hospital. The orthotopic bone-tumor model was established by injecting 143B-luc cells (2×10^5 in 20 μL PBS) in the cavum medullare of BALB/c nude mice tibia. The MR images were acquired on a Bruker 7.0 T magnet with Avance II hardware equipped with a 72 mm quadrature transmit/receive coil. The parameters for 7 T MRI are TR = 750.0 ms, TE = 12.6 ms, echo = 1/1, FOV = 6.91/3.12 cm, slice thickness = 2 mm, nex = 2 mm, matrix = 256 × 116. Two mice with orthotopic bone tumor were intravenously injected with 200 μl PDA/Fe and PDA-MOF-E-M (30 mg/kg, both concentrations calculated by the mass of PDA/Fe, Fe content in PDA/Fe was 5.3%), respectively. The MR images were collected before and 24 h after injection.

3.13. In vivo photothermal treatment of bone tumors

Male BALB/c nude mice (4 weeks of age) with an average body weight of 20 g were conducted in accordance with the National Institutes of Health Guidelines for the Care and Use of Laboratory Animals and approved by the Ethics Committee of Chinese PLA General Hospital. 143B-luc cells (2×10^5 cells in 20 μl phosphate buffer (PBS)) were transplanted into the lumen medulla of the tibia of nude mice. After two weeks, the mice were divided into five groups. Three groups of mice were given 100 μL PDA, PDA-MOF-E and PDA-MOF-E-M through caudal vein, respectively. Then, at 24 and 48 h after injection, the mice were irradiated with NIR with a power density of 3.6 W·cm-2 for 10 min. Second and third injections were given on the fourth and eighth day after the first injection, and the same NIR was given. Luminescent imaging of tumors was recorded before and after treatment using a small animal live imaging system (Lumina-II, Caliper Life Sciences, USA). The weight of the mice was recorded daily. Temperature and thermal images of tumor sites in mice were obtained using infrared thermography.

3.14. Treatment of malignant bone tumors by nanoparticles

The orthotopic osteosarcoma model was established using 143B cells as described above. The mice with similar luminescence intensities at tumor site were rationally divided into five groups (five mice in each group) and intravenously injected with 150 μL PBS, PDA, MOF, PDA-MOF-E and PDA-MOF-E-M respectively. The treatments were repeated every other day with a total number of six injections, and the mice were imaged and quantitatively analyzed by IVIS before the first injection, after the third and sixth injection, respectively. The circumference of tumor-bearing legs and the body weight of each mouse were recorded every day. The mice were sacrificed after treatment. The tumor-bearing legs were excised from the mice bearing osteosarcoma 143B tumor, and scanned by Siemens Biograph micro-CT (Skyscan 1076, Antwerp, Belgium). A CTVox program (Bruker micro-CT NV, Antwerp, Belgium) was employed to reconstruct the 3D structure of tibias.

3.15. In vivo three-dimensional (3D) microcomputed tomography (micro-CT) reconstruction of the tibia

Hind legs with tumors were isolated from the sacrificed mice after photothermal treatment. The hind legs of mice were placed in a scanning rack and analyzed using the Siemens Biograph 3D micro-CT device (Skyscan 1076, Antwerp, Belgium). After scanning, the 3D model was reconstructed and evaluated using the CTVox program (Bruker micro-CT NV, Antwerp, Belgium).

3.16. Statistical analysis

All data came from the results of three independent repeated experiments. Graphpad Prism 10.0 was used for data processing and statistical analysis. The one-way-ANOVA was performed to statistical analysis of multiple groups under the premise of homogeneity of variance. All statistical data was displayed as Mean ± SEM. *$p < 0.05$, **$p < 0.01$ and ***$p < 0.001$.

4. Conclusion

In summary, a ferroptosis-targeted nanoparticle, PDA-MOF-E-M, combined with PTT was hereby reported for the OS treatment. The PDA-MOF-E-M utilized Fe-MOFs to create a cellular iron-rich environment, took the erastin as a ferroptosis inducer, and ensured the targeted delivery to osteosarcoma cells through cell membrane encapsulation. PDA-MOF-E-M behaved well in physical and chemical characteristics, including particle size distribution, spectral absorption, thermal and pH stability. In terms of biological functions, PDA-MOF-E-M could induce the process of ferroptosis in osteosarcoma cells owning to Fe-MOFS and erastin, enhance efficacy of PTT benefit from PDA, and improve the bioavailability thanks to the cell membrane encapsulation. In the tibia tumor bearing mice, PDA-MOF-E-M could target osteosarcoma, inhibit osteoclast differentiation and suppress osteosarcoma growth.

These results indicated that PDA-MOF-E-M could be performed as a nuclear magnetic resonance imaging contrast agent to guide the treatment of osteosarcoma. Overall, this study provided a new therapeutic option for the treatment of malignant bone tumors.

Ethics approval and consent to participate

Study protocols were approved by the Ethics Committee of Chinese PLA General Hospital. Informed consent was obtained from all participants included in this study according to the committee regulations.

Consent for publication

All authors agree with the content of the manuscript.

Funding

This work was supported by the National Natural Science Foundation of China (Grant No. 82373297).

CRediT authorship contribution statement

Yu-jie Liu: Writing – original draft, Validation, Investigation, Formal analysis. **Su-he Dong:** Writing – original draft, Investigation, Conceptualization. **Wen-hao Hu:** Investigation. **Qiao-ling Chen:** Formal analysis. **Shao-fu Zhang:** Investigation. **Kai Song:** Investigation. **Zhen-**

chuan Han: Validation. **Meng-meng Li:** Validation. **Zhi-tao Han:** Writing – review & editing, Supervision. **Wei-bo Liu:** Validation, Supervision, Data curation. **Xue-song Zhang:** Writing – review & editing, Conceptualization.

Declaration of competing interest

We declare that we have no financial and personal relationships with other people or organizations that can inappropriately influence our work, there is no professional or other personal interest of any nature or kind in any product, service and/or company that could be construed as influencing the position presented in, or the review of, the manuscript entitled, '**A multifunctional biomimetic nanoplatform for image-guideded photothermal-ferroptotic synergistic osteosarcoma therapy**'.

Appendix A. Supplementary data

Supplementary data to this article can be found online at https://doi.org/10.1016/j.bioactmat.2024.02.007.

References

[1] J. Gill, R. Gorlick, Advancing therapy for osteosarcoma, Nat. Rev. Clin. Oncol. 18 (10) (2021) 609–624.
[2] P.S. Meltzer, L.J. Helman, New horizons in the treatment of osteosarcoma, N. Engl. J. Med. 385 (22) (2021) 2066–2076.
[3] C. Yang, Y. Tian, F. Zhao, et al., Bone microenvironment and osteosarcoma metastasis, Int. J. Mol. Sci. 21 (19) (2020).
[4] Y. Haridy, F. Witzmann, P. Asbach, et al., Triassic cancer-osteosarcoma in a 240-million-year-old stem-turtle, JAMA Oncol. 5 (3) (2019) 425–426.
[5] F.H.J. Kaptein, M.A.M. Stals, R.E. Evenhuis, et al., Risk of venous thromboembolism and major bleeding in the clinical course of osteosarcoma and Ewing sarcoma, Thromb. Res. 221 (2023) 19–25.
[6] L.M. Kelley, M. Schlegel, S. Hecker-Nolting, et al., Pathological fracture and prognosis of high-grade osteosarcoma of the extremities: an analysis of 2,847 consecutive cooperative osteosarcoma study group (COSS) patients, J. Clin. Oncol. : Offic. J. American Soc. Clin. Oncol. 38 (8) (2020) 823–833.
[7] W. Liu, X. Xie, Y. Qi, et al., Exploration of immune-related gene expression in osteosarcoma and association with outcomes, JAMA Netw. Open 4 (8) (2021) e2119132.
[8] K.H. Lu, E.W. Lu, C.W. Lin, et al., New insights into molecular and cellular mechanisms of zoledronate in human osteosarcoma, Pharmacol. Therapeut. 214 (2020) 107611.
[9] J. Fu, T. Li, Y. Yang, et al., Activatable nanomedicine for overcoming hypoxia-induced resistance to chemotherapy and inhibiting tumor growth by inducing collaborative apoptosis and ferroptosis in solid tumors, Biomaterials 268 (2021) 120537.
[10] Y. Yuan, Z. Mei, Z. Qu, et al., Exosomes secreted from cardiomyocytes suppress the sensitivity of tumor ferroptosis in ischemic heart failure, Signal Transduct. Targeted Ther. 8 (1) (2023) 121.
[11] W. Lin, J. Huang, S. Guo, et al., A tunable fluorescent probe for superoxide anion detection during inflammation caused by Treponema pallidum, J. Mater. Chem. B 11 (20) (2023) 4523–4528.
[12] W. Tao, N. Wang, J. Ruan, et al., Enhanced ROS-boosted phototherapy against pancreatic cancer via Nrf2-mediated stress-defense pathway suppression and ferroptosis induction, ACS Appl. Mater. Interfaces 14 (5) (2022) 6404–6416.
[13] Y. Xie, W. Hou, X. Song, et al., Ferroptosis: process and function, Cell Death Differ. 23 (3) (2016) 369–379.
[14] F. Zhan, Y. Zhang, Q. Zuo, et al., YAP knockdown in combination with ferroptosis induction increases the sensitivity of HOS human osteosarcoma cells to pyropheophorbide-α methyl ester-mediated photodynamic therapy, Photodiagnosis Photodyn. Ther. 39 (2022) 102964.
[15] X. Hu, R. Li, W. Wu, et al., A Fe(III)-porphyrin-oxaliplatin(IV) nanoplatform for enhanced ferroptosis and combined therapy, J. Contr. Release : official journal of the Controlled Release Society 348 (2022) 660–671.
[16] C. Wang, J. Wang, X. Pan, et al., Reversing ferroptosis resistance by MOFs through regulation intracellular redox homeostasis, Asian J. Pharm. Sci. 18 (1) (2023) 100770.
[17] K.H. Wong, D. Yang, S. Chen, et al., Development of nanoscale drug delivery systems of dihydroartemisinin for cancer therapy: a review, Asian J. Pharm. Sci. 17 (4) (2022) 475–490.
[18] L. Tang, L. Wang, X. Yang, et al., Poly(N-isopropylacrylamide)-based smart hydrogels: design, properties and applications, Prog. Mater. Sci. 115 (2021) 100702.
[19] Y. Chen, M. Su, L. Jia, et al., Synergistic chemo-photothermal and ferroptosis therapy of polydopamine nanoparticles for esophageal cancer, Nanomedicine 17 (16) (2022) 1115–1130.
[20] Z. Chen, Z. Li, C. Li, et al., Manganese-containing polydopamine nanoparticles as theranostic agents for magnetic resonance imaging and photothermal/chemodynamic combined ferroptosis therapy treating gastric cancer, Drug Deliv. 29 (1) (2022) 1201–1211.
[21] H. Deng, J. Zhang, Y. Yang, et al., Chemodynamic and photothermal combination therapy based on dual-modified metal-organic framework for inducing tumor ferroptosis/pyroptosis, ACS Appl. Mater. Interfaces 14 (21) (2022) 24089–24101.
[22] A.J. Gormley, N. Larson, S. Sadekar, et al., Guided delivery of polymer therapeutics using plasmonic photothermal therapy, Nano Today 7 (3) (2012) 158–167.
[23] P. Lin, Y. Xue, X. Mu, et al., Tumor customized 2D supramolecular nanodiscs for ultralong tumor retention and precise photothermal therapy of highly heterogeneous cancers, Small 18 (21) (2022) e2200179.
[24] K. Liu, Y. Liao, Z. Zhou, et al., Photothermal-triggered immunogenic nanotherapeutics for optimizing osteosarcoma therapy by synergizing innate and adaptive immunity, Biomaterials 282 (2022) 121383.
[25] H. Lou, A. Ji, C. Qu, et al., A small-molecule based organic nanoparticle for photothermal therapy and near-infrared-IIb imaging, ACS Appl. Mater. Interfaces 14 (31) (2022) 35454–35465.
[26] S. Liang, G. Liao, W. Zhu, et al., Manganese-based hollow nanoplatforms for MR imaging-guided cancer therapies, Biomater. Res. 26 (1) (2022) 32.
[27] Y. Zou, H. Jin, F. Sun, et al., Design and synthesis of a lead sulfide based nanotheranostic agent for computer tomography/magnetic resonance dual-mode-bioimaging-guided photothermal therapy, ACS Appl. Nano Mater. 1 (5) (2018) 2294–2305.
[28] T.M.T. Vo, S. Mondal, V.T. Nguyen, et al., Rice starch coated iron oxide nanoparticles: a theranostic probe for photoacoustic imaging-guided photothermal cancer therapy, Int. J. Biol. Macromol. 183 (2021) 55–67.
[29] Z. Mo, Q. Li, K. Zhao, et al., A nanoarchitectonic approach enables triple modal synergistic therapies to enhance antitumor effects, ACS Appl. Mater. Interfaces 14 (8) (2022) 10001–10014.
[30] M. Chang, Z. Hou, M. Wang, et al., Single-Atom Pd nanozyme for ferroptosis-boosted mild-temperature photothermal therapy, Angew. Chem. 60 (23) (2021) 12971–12979.
[31] C. DU, X. Wu, M. He, et al., Polymeric photothermal agents for cancer therapy: recent progress and clinical potential, J. Mater. Chem. B 9 (6) (2021) 1478–1490.
[32] F. Zeng, L. Tang, Q. Zhang, et al., Coordinating the mechanisms of action of ferroptosis and the photothermal effect for cancer theranostics, Angew. Chem. 61 (13) (2022) e202112925.
[33] J. Kolosnjaj-Tabi, S. Kralj, E. Griseti, et al., Magnetic silica-coated iron oxide nanochains as photothermal agents, disrupting the extracellular matrix, and eradicating cancer cells, Cancers 11 (12) (2019).
[34] Z. Qin, M. Qiu, Q. Zhang, et al., Development of copper vacancy defects in a silver-doped CuS nanoplatform for high-efficiency photothermal-chemodynamic synergistic antitumor therapy, J. Mater. Chem. B 9 (42) (2021) 8882–8896.
[35] L.P. Zhao, S.Y. Chen, R.R. Zheng, et al., Photodynamic therapy initiated ferrotherapy of self-delivery nanomedicine to amplify lipid peroxidation via GPX4 inactivation, ACS Appl. Mater. Interfaces. 14 (48) (2022) 53501–53510.
[36] G. Li, Z. Song, Y. Ru, et al., Small-molecule nanoprodrug with high drug loading and EGFR, PI3K/AKT dual-inhibiting properties for bladder cancer treatment, Exploration (Beijing) 3 (5) (2023) 20220141.
[37] L. Zhang, G. Oudeng, F. Wen, et al., Recent advances in near-infrared-II hollow nanoplatforms for photothermal-based cancer treatment, Biomater. Res. 26 (1) (2022) 61.
[38] T. Bedhiafi, S. Idoudi, A.A. Alhams, et al., Applications of polydopaminic nanomaterials in mucosal drug delivery, J. Contr. Release : Off. J. Controlled Release Soc. 353 (2023) 842–849.
[39] X. He, E. Obeng, X. Sun, et al., Polydopamine, harness of the antibacterial potentials-A review, Materials today Bio. 15 (2022) 100329.
[40] A. Jin, Y. Wang, K. Lin, et al., Nanoparticles modified by polydopamine: working as "drug" carriers, Bioact. Mater. 5 (3) (2020) 522–541.
[41] M. Kim, R. Xin, J. Earnshaw, et al., MOF-derived nanoporous carbons with diverse tunable nanoarchitectures, Nat. Protoc. 17 (12) (2022) 2990–3027.
[42] Z. Mo, M. Qiu, K. Zhao, et al., Multifunctional phototheranostic nanoplatform based on polydopamine-manganese dioxide-IR780 iodide for effective magnetic resonance imaging-guided synergistic photodynamic/photothermal therapy, J. Colloid Interface Sci. 611 (2022) 193–204.
[43] Z. Mo, X. Pan, X. Pan, et al., MOF(Fe)-derived composites as a unique nanoplatform for chemo-photodynamic tumor therapy, J/OL] 10 (42) (2022) 8760–8770, https://doi.org/10.1039/d2tb01691e.
[44] C. Li, J. Yang, R. Xu, et al., Progress and prospects of electrochemiluminescence biosensors based on porous nanomaterials, Biosensors 12 (7) (2022).
[45] Y. Zou, F. Sun, C. Liu, et al., A novel nanotheranostic agent for dual-mode imaging-guided cancer therapy based on europium complexes-grafted-oxidative dopamine, Chem. Eng. J. 357 (2019) 237–247.
[46] S. Xue, X. Zhou, W. Sang, et al., Cartilage-targeting peptide-modified dual-drug delivery nanoplatform with NIR laser response for osteoarthritis therapy, Bioact. Mater. 6 (8) (2021) 2372–2389.
[47] R. Chen, C. Zhu, Y. Fan, et al., Polydopamine-based multifunctional platform for combined photothermal therapy, chemotherapy, and immunotherapy in malignant tumor treatment, ACS Appl. Bio Mater. 2 (2) (2019) 874–883.
[48] G. Liao, L. Zhang, C. Li, et al., Emerging carbon-supported single-atom catalysts for biomedical applications, Matter 5 (10) (2022) 3341–3374.
[49] A. Singh, A.K. Yadawa, S. Chaturvedi, et al., Mechanism for antiParkinsonian effect of resveratrol: involvement of transporters, synaptic proteins, dendrite arborization, biochemical alterations, ER stress and apoptosis, Food Chem. Toxicol. : an Int. J. Published British Industrial Biol. Res. Assoc. 155 (2021) 112433.

[50] Y. Yang, Y. He, Y. Jin, et al., Amino acids in endoplasmic reticulum stress and redox signaling, Adv. Exp. Med. Biol. 1332 (2021) 35–49.
[51] H. Huang, Z. Ye, Z. Li, et al., Employing machine learning using ferroptosis-related genes to construct a prognosis model for patients with osteosarcoma, Front. Genet. 14 (2023) 1099272.
[52] W.C. Dougall, M. Glaccum, K. Charrier, et al., RANK is essential for osteoclast and lymph node development, Genes Dev. 13 (18) (1999) 2412–2424.
[53] T. Efferth, F. Oesch, The immunosuppressive activity of artemisinin-type drugs towards inflammatory and autoimmune diseases, Med. Res. Rev. 41 (6) (2021) 3023–3061.
[54] X. Yu, J.T. Yustein, J. Xu, Research models and mesenchymal/epithelial plasticity of osteosarcoma, Cell Biosci. 11 (1) (2021) 94.
[55] W.B. Liu, S.H. Dong, W.H. Hu, et al., A simple, universal and multifunctional template agent for personalized treatment of bone tumors, Bioact. Mater. 12 (2022) 292–302.
[56] Y. Yan, X. Gao, S. Zhang, et al., A carboxyl-terminated dendrimer enables osteolytic lesion targeting and photothermal ablation of malignant bone tumors, ACS Appl. Mater. Interfaces. 11 (1) (2019) 160–168.